Parameterization and Evaluation of Nonhydrostatic Effect in the Orographic Gravity Wave Drag in China Meteorological Administration Global Forecast System (CMA-GFS) v4.0 Model

Rongrong ZHANG[1,2,3], Zhenzhen AI[1], Xin XU[1], Haile XUE[4,5], Qiying CHEN[4,5]

[1]State Key Laboratory of Severe Weather Meteorological Science and Technology, Key laboratory of Mesoscale Severe Weather/Ministry of Education, School of Atmospheric Sciences, Nanjing University, Nanjing 210023, China
[2]Jiangsu Meteorological Observatory, Jiangsu Meteorological Bureau, Nanjing 210008, China
[3]Jiangsu Key Laboratory of Severe Storm Disaster Risk/Key Laboratory of Transportation Meteorology of CMA, Nanjing 210041, China
[4]State Key Laboratory of Severe Weather Meteorological Science and Technology, CMA Earth System Modeling and Prediction Centre, Beijing 100081, China
[5]Key Laboratory of Earth System Modeling and Prediction, China Meteorological Administration, Beijing 100081, China

Correspondence: Xin Xu (xinxu@nju.edu.cn) and Haile Xue (xuehl@cma.cn)

Abstract

The China Meteorological Administration Global Forecast System (CMA-GFS) v4.0 model was upgraded to a higher resolution of 0.125° in May 2023. To be compatible with its fine resolution, the parameterization scheme of orographic gravity wave drag (OGWD) in CAM-GFS is revised herein by accounting for the nonhydrostatic effect (NHE) on the wave momentum flux of subgrid-scale orographic gravity waves. The performance of the revised OGWD scheme is then evaluated for the 10-day medium-range forecast in December 2023. Results show that the revised OGWD scheme can better capture the large-scale circulation in the Northern Hemisphere (NH), particularly in the high latitudes. The easterly (westerly) wind biases in the NH polar stratosphere (troposphere) are decreased. The underestimation of East Asia subtropical jet is also alleviated. Quantitative evaluation shows that the revised OGWD scheme reduces both the mean bias and root mean square error of 500-hPa geopotential height in the NH after the 6th forecast day, reaching 11.59% and 5.06%, respectively, by day 10. The decrease of easterly biases in the polar stratosphere is owing to the weakening of stratospheric zonal OGWD by the NHE. For the decrease of westerly biases in the NH polar troposphere, it is due to the fact that the enhanced stratospheric winds suppress the upward propagation of Rossby waves into the stratosphere, resulting in greater convergence of Eliassen-Palm flux in the mid-upper troposphere.

Keywords: orographic gravity wave drag, parameterization, global NWP medium-range forecast

1. Introduction

Orographic gravity wave drag (OGWD) is an important process in atmospheric dynamics, arising from the interaction of airflow with complex terrain (Kim et al., 2003; Teixeira, 2014). When airstream flows over mountains, it generates orographic gravity waves (OGWs) which propagate vertically. As these waves break, they generate OGWD on the high-level atmosphere (Fritts and Alexander, 2003). The OGWD plays a crucial role in driving the atmospheric circulation, influencing both tropospheric and stratospheric dynamics (Alexander et al., 2010).

In numerical weather prediction (NWP) and climate models, the OGWD is typically a subgrid-scale process which needs to be parameterized. Various OGWD parameterization schemes have been developed over the past few decades (e.g., Palmer et al., 1986; McFarlane, 1987; Kim and Arakawa, 1995; Lott and Miller, 1997; Scinocca and McFarlane, 2000; Kim and Doyle, 2005) based on both linear and nonlinear OGW dynamics. Their implementation has been shown to help alleviate the systematic biases in both NWP and climate models, ranging from general circulation to regional climate and weather (e.g., Kim, 2007; McLandress et al., 2012; Choi and Hong, 2015; Zhong and Chen, 2015; Chen et al., 2016; Lu et al., 2020; Zhang et al., 2020; Li et al., 2023; Xu et al., 2023; Wei et al., 2025).

While accurate representation of OGWD is essential for weather forecast and climate simulation/projection, traditional OGWD parameterization schemes rely on the assumption of hydrostatic balance which can significantly simplify the formulae of OGW dynamics. This assumption is appropriate for coarse-resolution numerical models where subgrid-scale OGWs are dominated by hydrostatic GWs as the dominant subgrid

68 "mountains" are large. However, as the model resolution increases, the hydrostatic
69 assumption becomes less valid because the subgrid-scale orography (SSO) becomes
70 smaller, so that the unresolved GWs have shorter wavelengths. In this situation, the
71 nonhydrostatic effects (NHEs) will exert remarkable influences on the subgrid-scale
72 OGWs. Compared with hydrostatic OGWs, nonhydrostatic OGWs experience stronger
73 horizontal dispersion of wave energy, which reduces wave amplitude and can suppress
74 wave breaking and momentum deposition into the mean flow (Smith, 1979; Klemp and
75 Durran, 1983; Zängl, 2003). These NHEs are thus critical for accurately representing
76 the dynamical impacts of subgrid-scale OGWs in high-resolution models, e.g., the
77 *state-of-the-art* global NWP models.

78 Recently, Xu et al. (2021) theoretically derived the analytical expressions for
79 the surface wave momentum flux (WMF) of nonhydrostatic OGWs generated by
80 idealized three-dimensional orography. They found that the degree of nonhydrostaticity
81 can be measured by a nondimensional parameter of Froude number which is equal to
82 the wind speed over the mountain half width and buoyancy frequency, i.e., the inverse
83 of the nondimensional half-width Na/U (e.g., Zängl, 2003). Physically, this parameter
84 represents the ratio between the period of buoyancy oscillation and the time for airflow
85 travelling through the mountain. The larger the horizontal Froude number, the more
86 important the NHE is. Based upon the theoretical study, Xu et al. (2023, 2024) revised
87 the OGWD parameterization scheme developed by Kim and Doyle (2005, hereafter
88 KD05) by accounting for the NHE on the surface WMF of upward-propagating OGWs.
89 Then the new OGWD scheme was implemented in the Model for Prediction Across
90 Scales (MPAS), which was shown to improve the seasonal simulation of the

stratospheric polar night jet and reduce the wet biases over the western Tibetan Plateau in winter. Li et al. (2024) further evaluated the revised OGWD scheme in the Weather Research and Forecasting (WRF) model for short-range forecast of Northeast China cold vortices (NECVs). The underestimation of the NECV intensity (in terms of minimum 500-hPa geopotential height) is alleviated as the NHE decreases the lower-tropospheric OGWD.

The Global Forecast System in China Meteorological Administration (CMA-GFS), the global component of the Global/Regional Assimilation and Prediction System (GRAPES), was developed in early 2000s (Shen et al., 2017). Operationally running at the CMA Earth System Modeling and Prediction Center, the CMA-GFS was upgraded to a new version of v4.0 in May 2023, with its horizontal resolution increasing from 0.25° to 0.125° (about 13 km), along with many other improvements in the model dynamics and physics (Shen et al., 2023). For instance, the convective triggering function and quasi-equilibrium closure conditions are improved to reduce biases in tropics and enhance forecast skill of precipitation in East Asia. In CMA-GFS, three components of subgrid scale orography effects have been implemented, i.e., the blocking-flow drag (BFD), the OGWD and turbulent orographic form drag (TOFD). The TOFD scheme was implemented CMA-GFS based on Beljaars et al. (2004) and Xue et al. (2011) and will not be further discussed as it is not relevant to the NHE effect studied in this study. The BFD component based on Lott and Millor (1997, hereafter LM97) and OGWD component from Kim and Arakawa (1995, hereafter KA95) were implemented in CMA-GFS similar to that in Alpert (2004) and was described in Chen et al. (2016). It is noticed that in the existing implementation, nonhydrostatic effects are

114 only partly reflected through a Scorer-parameter-based partitioning of the momentum
115 stress when the model grid point is located downstream of the subgrid orography. However,
116 the launch-level surface WMF itself still follows the original hydrostatic KA95 formulation.
117 In order to be compatible with its high resolution, this hydrostatic OGWD
118 parameterization scheme needs to be upgraded to account for the NHE.

119 Note that the present study extends the evaluation of the nonhydrostatic OGWD
120 scheme in the MPAS model presented in Xu et al. (2024) by transitioning it into a
121 practical, operational NWP. Although Xu et al. (2024) demonstrated the beneficial
122 impact of the revised OGWD scheme for long-term, large-scale circulation simulations,
123 its performance and value within a state-of-the-art, high-resolution global forecasting
124 system performing routine medium-range forecasts had not been tested. This work
125 provides this critical assessment using the CMA-GFS v4.0 model, with a specific focus
126 on forecast skill improvements for several quantitative metrics. The primary advance
127 lies in evaluating the revised OGWD scheme in reducing systematic forecast biases on
128 timescales directly relevant to weather prediction (1-10 days), demonstrating the
129 tangible benefits of incorporating nonhydrostatic effects to improve medium-range
130 weather forecasting accuracy.

131 The remainder of the paper is organized as follows. Section 2 firstly introduces
132 the revision of the OGWD parameterization scheme and then describes the setup of the
133 numerical experiments. Section 3 gives an overall evaluation for the medium-range
134 forecast of large-scale atmospheric circulation by the CMA-GFS model. The NHE
135 effects on parameterized OGWD and large-scale circulation are examined in section 4.
136 Finally, the paper is summarized in section 5 along with discussions.

2. OGWD parameterization scheme and numerical experiments

a. Revision of the KA95 OGWD parameterization scheme

The KA95 OGWD considers various aspects of the SSO including its standard deviation (σ_h), orographic asymmetry (*OA*) and orographic convexity (*OC*). The surface WMF of OGWs is given by

$$\tau_0 = \rho_0 E \frac{m}{\lambda_{eff}} G \frac{|V_0|^3}{N_0}, \quad (1)$$

where

$$E = (OA+2)^{C_E \frac{Fr_0}{Fr_c}}, m = (1+L_x)^{OA+1}, G = \frac{Fr_0^2}{Fr_0^2 + C_G OC^{-1}}, Fr_0 = \frac{\sigma_h N_L}{|\mathbf{V}_L|}. \quad (2)$$

The variables ρ_0, $|\boldsymbol{V_0}|$ and N_0 are the low-level (from the surface to $2\sigma_h$) mean air density, horizontal wind speed and buoyancy frequency. The parameter *m* denotes the "number of mountains" within the grid cell, characterizing the total volume of SSO associated with the orography length (L_x). The coefficient λ_{eff} acts as a tunable parameter denoting the effective grid length. The transition function *G* is an enhancement factor for sharp mountains as OC is large. This scheme also considers the effects of low-level wave breaking and/or lee wave trapping through the factor *E*, which is a function of the shape and location of the SSO within the model grid cell (i.e., *OA*), and the flow nonlinearity (i.e., $Fr_0 = \frac{Nh_0}{U}$). The two empirical constants are set to C_E = 0.8 and C_G = 0.5, which are obtained empirically through a series of numerical simulations conducted in Kim and Arakawa (1995).

The surface WMF is transported upward level by level until reaching the model top or critical level. At each model level, airflow instability is checked according to the

158 hypothesis of wave saturation (Lindzen, 1981) and wave-breaking (Miller and Palmer,
159 1986).

160 Once the subgrid-scale OGWs saturate and break, they will exert a body force
161 on the mean flow through the deposition of wave momentum, namely,

162 $$\frac{d\boldsymbol{V}(z)}{dt} = \frac{1}{\rho(z)}\frac{\partial \boldsymbol{\tau}(z)}{\partial z}. \quad (3)$$

163 where $\boldsymbol{V}(z)$ and $\boldsymbol{\tau}(z)$ are the mean flow velocity and the WMF at height z, respectively.
164 Note that both the directions of $\boldsymbol{V}(z)$ and $\boldsymbol{\tau}(z)$ are parallel to the mean flow at the low
165 level (i.e., $\boldsymbol{V_L}$). Readers are referred to KA95 for more details about the scheme.

166 The hydrostatic KA95 scheme above is revised by taking into account the NHE
167 on the surface WMF of OGWs, i.e.,

168 $$\tilde{\tau} = \tau_0[1 + NHE(Fr)]. \quad (4)$$

169 $\tilde{\tau}$ represents the nonhydrostatic surface WMF, where the NHE correction depends only
170 on the horizontal Froude number $Fr = \frac{|\boldsymbol{V_0}|}{N_0 L_x}$

171 $$NHE(Fr) = -\frac{9}{8}Fr^2 + e^{-2Fr^{-1}}\left(-\frac{5}{4}Fr^{-2} - \frac{1}{2}Fr^{-1} + \frac{5}{4} + \frac{9}{4}Fr + \frac{9}{8}Fr^2\right). \quad (5)$$

172 Eq. (5) is adopted from Xu et al. (2021) for three-dimensional isotropic terrain. Specifically,
173 the nonhydrostatic correction is defined as the ratio of the analytically derived
174 nonhydrostatic surface WMF to its hydrostatic counterpart, which yields an algebraic
175 correction factor depending only on the horizontal Froude number. Note that the
176 horizontal Froude number is different from the traditional Froude number Fr_0 above
177 which measures the flow nonlinearity. While Xu et al. (2021) have derived the fully
178 NHE for anisotropic terrain, the expressions involve complicated integrals that are not
179 suitable for practical use in parameterization [cf. their Eqs. (14) to (17)]. Xu et al. (2021)

demonstrated that terrain anisotropy only has a very weak influence on the NHE, so the expression of NHE for isotropic terrain, i.e., Eq. (5), is used because of simplicity, since only algebraic manipulations are involved. This is in agreement with Xu et al. (2023, 2024) and Li et al. (2024).

b. Setup of numerical experiments

The CMA-GFSv4.0 dynamical core is based upon the nonhydrostatic and shallow atmospheric governing equations in spherical polar coordinates with full physics packages (Shen et al., 2020). It adopts a regular latitude-longitude grid of 0.125°× 0.125° with *C*-grid staggering. In the vertical, a terrain-following height-based grid is utilized along with Charney-Phillips staggering. There are 87 vertical levels, with the model top located at 73 km. For model physics, the Liu-Ma microphysics scheme (Ma et al., 2018) is employed, along with the RRTMG longwave and shortwave radiation schemes (Morcrette et al., 2008), the MRF planetary boundary layer scheme (Chen et al. 2020; Hong and Pan 1996), the CoLM land surface model (Dai et al., 2003), NSAS convection scheme (Han and Pan, 2011; Liu et al., 2015), the combined KA95 OGWD and LM97 FBD parameterization scheme (Chen et al., 2016), and modified Beljaars's TOFD scheme (Xue et al., 2011).

In order to examine the impact of the revised OGWD scheme on the medium-range forecast, two sets of numerical simulations (i.e., EXP_CTL and EXP_NHE) are conducted with different OGWD parameterization schemes, using the original KA95 scheme and the revised nonhydrostatic one, respectively. Both experiments consist of 31 individual forecasts, each initialized at 00 UTC for the days from 1 to 31 December 2023.

Herein, a winter month is chosen because the OGWD, which is mainly located in the Northern Hemisphere (NH) given the pronounced orography, is the strongest in this season (e.g., Xu et al. 2020; Lu et al. 2024). In each experiment, the CMA-GFS model is integrated for 10 days, i.e., medium-range forecast, with 6-hr output interval. The model initial conditions are derived from the 0.25° × 0.25° ECMWF Reanalysis v5 (ERA5) dataset (Hersbach et al., 2020), which are also used as reference for the evaluation of the CMA-GFS forecasts. Although the horizontal resolution of ERA5 is coarser than that of the CMA-GFS v4.0 simulations, ERA5 is adopted here as the verification reference because it is a dynamically consistent reanalysis constrained by a broad range of assimilated observations. In this study, ERA5 is not used to resolve the non-hydrostatic subgrid-scale orographic gravity waves themselves. Instead, it serves as a benchmark for evaluating the large-scale circulation response and medium-range forecast skill associated with the revised OGWD parameterization.

3. Evaluation of the medium-range forecast

a. Atmospheric circulation

Figure 1 shows the zonal-mean zonal wind composited from the day 10 forecast output of the 31 simulations initialized at 00 UTC on 1-31 December 2023. Accordingly, the valid times of these day-10 forecasts span 10 December 2023 to 10 January 2024 (i.e., the 10th day of the medium-range forecast). In the winter of NH, as revealed by the ERA5 reanalysis (Fig. 1a), there is a subtropical jet in the midlatitudes troposphere and stratosphere, with the jet core located at about 200 hPa and 30°N. The maximum zonal wind speed exceeds 35 m s^{-1}. In the stratosphere of high latitudes, there is another wind

maxima near 1 hPa and 60°N, which is the well-known polar-night jet (e.g., Kim, 2007).. In the Southern Hemisphere (SH), which is in summer, there is also a upper tropospheric lower stratospheric jet but relatively weaker and lower than in the NH. The SH jet core is located at about 50°S, with a secondary one near 30°S. During austral summer, the SH stratosphere is dominated by easterlies, which is distinctly different from the NH. With a center located near 1 hPa and 20°S, the stratospheric easterlies extend downward and equatorward to the tropics. An easterly jet of over -30 m s^{-1} can be found near 20 hPa and 5°S.

Figure 1b is similar to Figure 1a but for the zonal-mean zonal winds obtained in the EXP_CTL experiment. In general, the CMA-GFS model can capture the overall pattern of the zonal-mean zonal winds, such as the tropospheric westerly jets in both hemispheres and the easterly winds in the SH stratosphere. The polar night jet in the NH, however, is underestimated by the model, with the jet core shifted southward by about 10 latitudes. As shown in Fig. 1c, there are notable easterly biases of over -5 m s^{-1} in the stratosphere of the NH high latitudes (north of 50°N). By contrast, westerly biases are present in the upper stratosphere of the NH midlatitudes (25°N-50°N) which can exceed 10 m s^{-1}, extending downward and equatorward to the lower stratosphere of the tropics. Similarly, the zonal-mean zonal winds in the NH troposphere are overestimated in the Arctic region, but with easterly biases in the mid-lower latitudes. In the SH, the stratospheric easterlies are shifted northward, leading to westerly biases in the mid-lower latitudes (40°S-5°S) and easterly biases in the tropics and lower latitudes of the NH (5°S-20°N). In the high latitudes, there are predominantly easterly

biases in both troposphere and stratosphere except in the upper stratosphere over the polar cap.

When taking into account the NHE in the OGWD parameterization scheme, the CMA-GFS model can better capture the large-scale circulation. Figure 1d presents the differences between the zonal-mean zonal winds in the two numerical experiments (i.e., EXP_NHE minus EXP_CTL). In the stratosphere above ~10 hPa, positive and negative wind differences are found to the north and south of 60°N, respectively, which are just opposed to the wind biases in Figure 1c. It suggests that both the magnitude and location of the polar night jet are improved. For example, the NH easterly biases in the mid-upper stratosphere (~10 hPa to 1 hPa) are reduced by about 3%. The westerly biases in the troposphere of Arctica region are also reduced, which reaches up to about 42% of the total bias. At the same time, the easterly wind biases in the mid-latitude troposphere have also reduced.

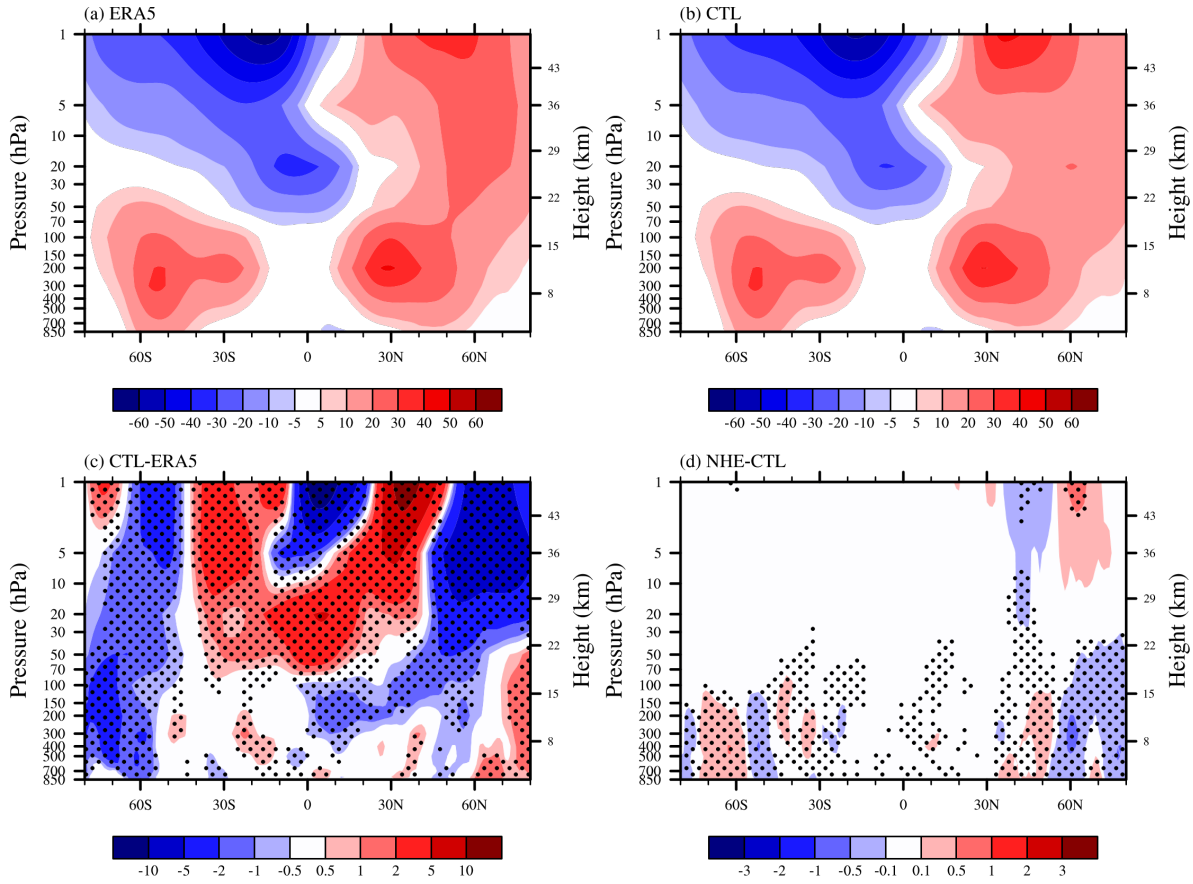

Figure 1. Vertical distributions of zonal-mean zonal wind (units: m s^{-1}) averaged in the period of 10 December 2023 to 10 January 2024 obtained from (a) ERA5 and (b) EXP_CTL, with their difference (i.e., EXP_CTL minus ERA5) given in (c). (d) is similar to (c) but for the difference between the two experiments of EXP_NHE and EXP_CTL (i.e., EXP_NHE minus EXP_CTL). Stippling in (c) and (d) denote differences statistically significant at the 95% confidence level.

For the zonal-mean zonal wind biases in the SH stratosphere, they are hardly alleviated, however. This is because the stratospheric OGWD is very weak in summer (see Fig. 5a of Xu et al. 2024; see also Fig. 3 below), given the absorption of OGWs at the critical level (Booker and Bretherton, 1967), that is, the zero-wind level between the tropospheric westerlies and the stratospheric easterlies (Fig. 1a). The easterly biases in the troposphere of the high latitudes are reduced, especially around 60°S.

Although there is no significant improvement for the zonal-mean zonal wind in the NH mid-lower latitudes (Fig. 1d), the wind circulation can be improved regionally, such as the East Asia subtropical jet (EASJ). Figure 2a shows the horizontal wind field and speed at 200 hPa averaged in the period of 10 December 2023 to 10 January 2024 from the ERA5 reanalysis. In boreal winter, the EASJ stretches from about 110°E to 160°E in the latitudes between about 25°N and 45°N. The jet core is located near Japan, showing a high wind speed of over 70 m s^{-1}. The simulated EASJ in the EXP_CTL experiment generally aligns well with the ERA5 reanalysis, in terms of its location and orientation (Fig. 2b). But the jet intensity is underestimated, showing easterly biases of over -4 m s^{-1} (Fig. 2c). In the EXP_NHE experiment, the underestimation of the EASJ is alleviated, with the mean bias decreased by about 6% (Fig. 2d).

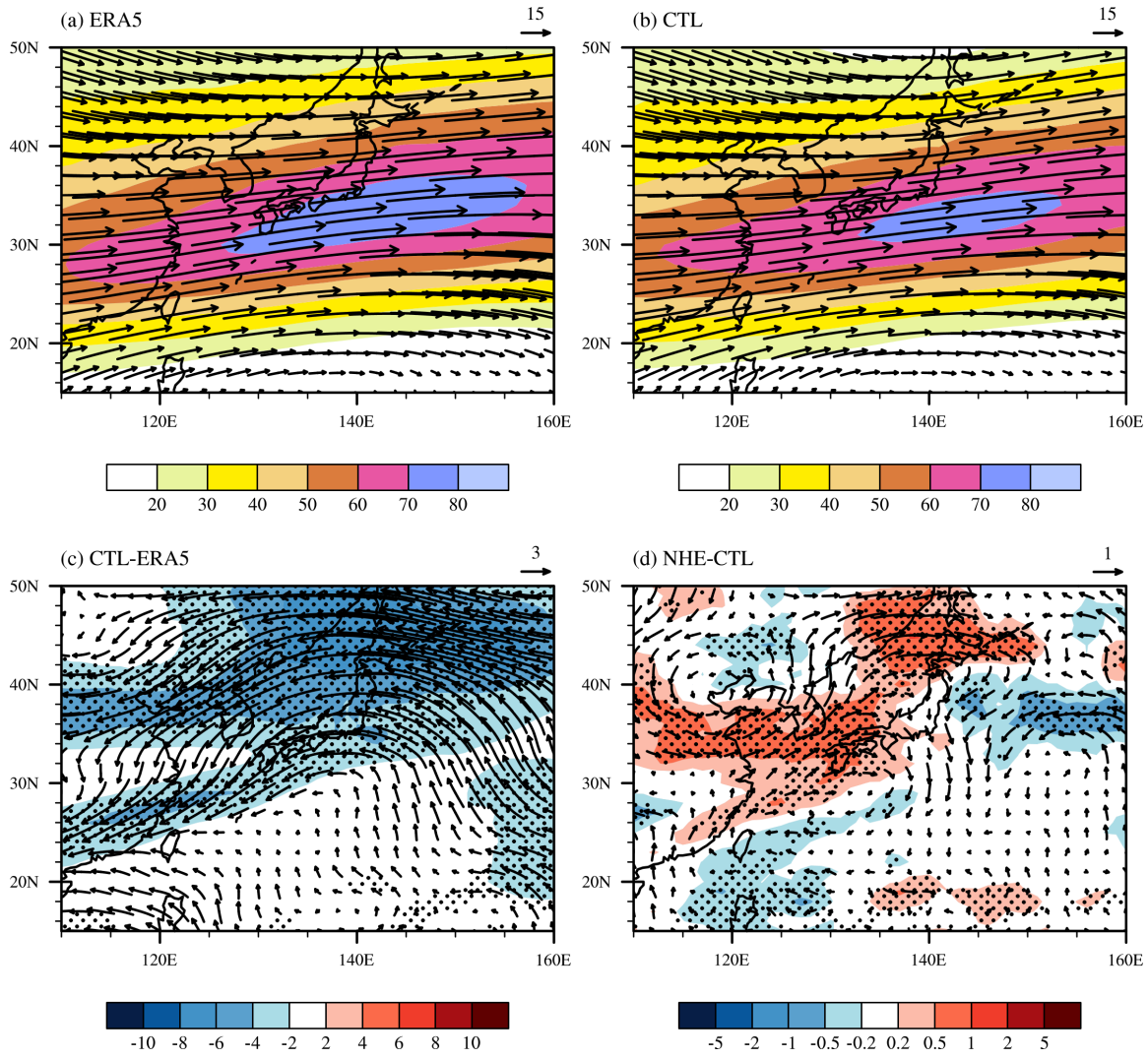

Figure 2. Horizontal distributions of wind speed (shading; units: m s^{-1}) and wind filed (arrow) at 200 hPa averaged in the period of 10 December 2023 to 10 January 2024 obtained from (a) ERA5 and (b) EXP_CTL, with their difference (i.e., EXP_CTL minus ERA5) given in (c). (d) is similar to (c) but for the difference between the two experiments of EXP_NHE and EXP_CTL (i.e., EXP_NHE minus EXP_CTL). Stippling in (c) and (d) denote differences statistically significant at the 95% confidence level.

b. Quantitative evaluation of forecast skills

For medium-range forecast, the wind circulation in the troposphere is often of greater interest than in the stratosphere. To better evaluate the performance of the revised OGWD scheme, Figures 3a and 3b depict the mean bias (MB) and root mean square error (RMSE) for the 500 hPa geopotential height (GPH500) in the two experiments. Herein, we are interested in the NH because of the relatively weak wind differences in the SH (Fig. 1d) which is mainly covered by the ocean. Moreover, as will be shown below, the parameterized OGWD changes little in the SH.

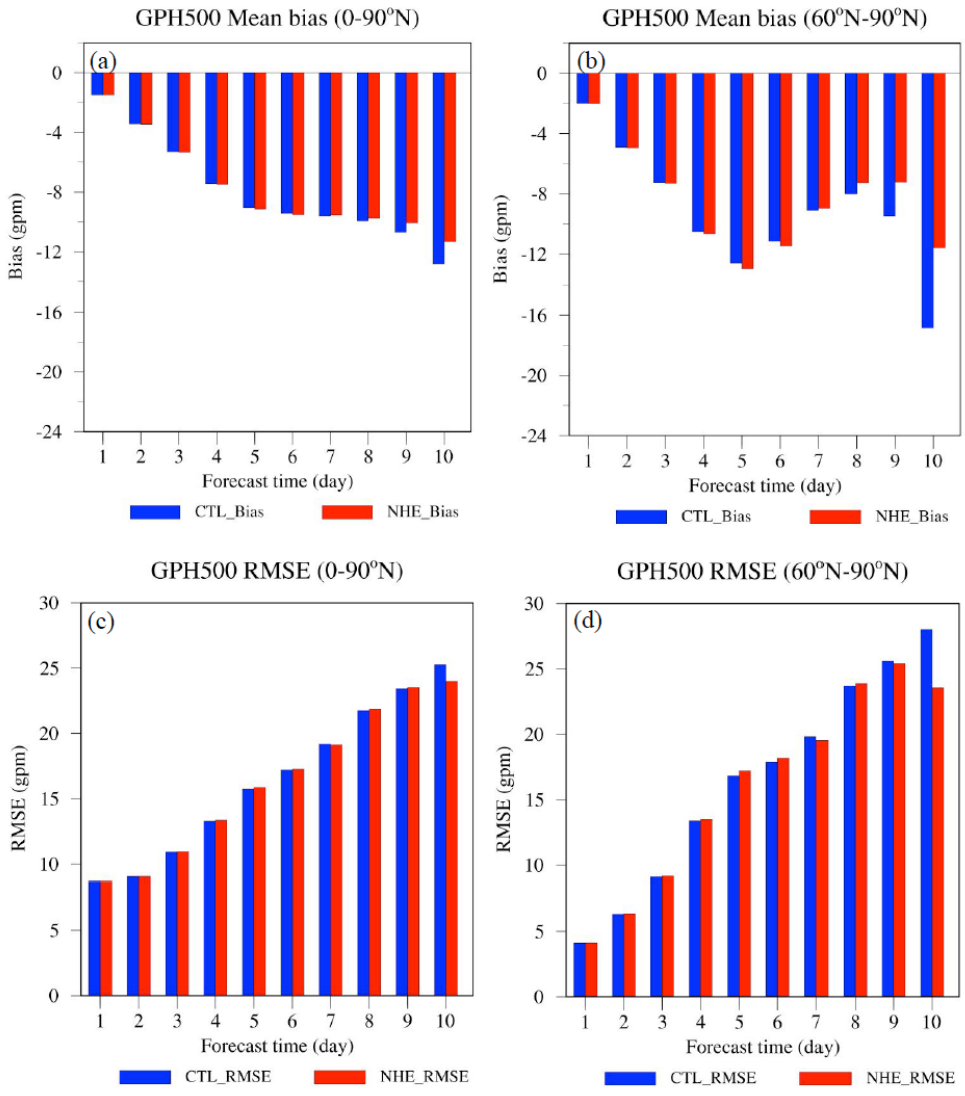

Figure 3. (a) Mean bias and (c) RMSE of the GPH500 in the NH at different forecast lead time. (b) and (d) are similar to (a) and (c) but in the region north of 60°N.

In both experiments, the model GPH500 is lower than the ERA5 reanalysis, with the MB and RMSE increasing with the forecast lead time (Figs. 3a, 3c). The GPH500 shows obvious underestimation in the EXP_CTL experiment which are significantly reduced in EXP_NHE. This improvement is particularly evident in high latitudes north of 60°N which is overall statistically significant at the 95% confidence level (Figs. 4a, 4b). Compared to EXP_CTL, EXP_NHE exhibits even greater MB and RMSE of GPH500 till the 6th forecast day. Nevertheless, both the MB and RMSE of the GPH500 decrease quickly afterwards, which are reduced by 11.59% and 5.06%, respectively, at the 10th day of the forecast (Table 1). Greater improvements are found for the GPH500 between 60°N and 90°N, the MB and RMSE of which are decreased by 31.18% and 15.93%, respectively, at the 10th forecast day (Table 1). All the values shown in Table 1 are statistically significant at the 95% confidence level. For the total 10 forecast days as a whole, the MB and RMSE of GPH500 are separately reduced by 2.6% and 0.52 %, indicating an overall improvement in the simulation of the large-scale circulation in the NH when using the revised OGWD scheme (see Table 2).

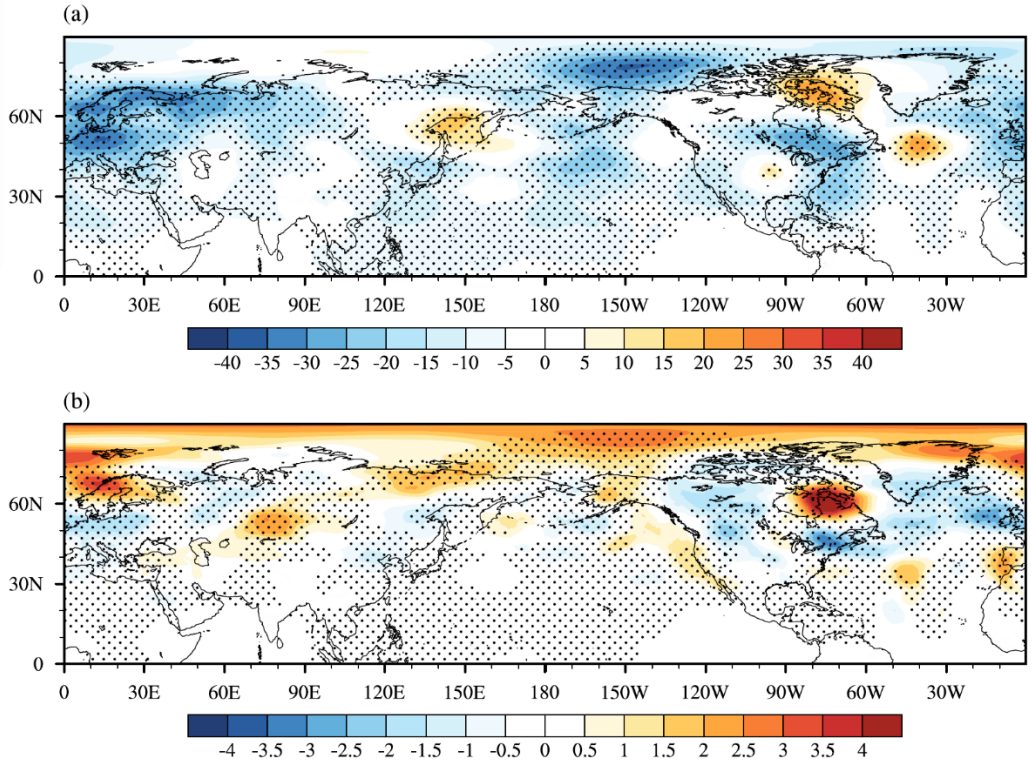

Figure 4. (a) Mean biases of GPH500 (shading; units: gpm) in EXP_CTL experiment as compared to ERA5 averaged over the ten forecast days. (b) is similar to (a) but for the differences between the GPH500 (shading; units: gpm) in EXP_CTL and EXP_NHE experiments (i.e., EXP_NHE minus EXP_CTL). Stippling in (a) and (b) denote differences statistically significant at the 95% confidence level.

Table 1. Mean bias and RMSE of the 500-hPa geopotential height (GPH500) and sea level pressure (SLP) at the 10th forecast day

		Mean Bias			RMSE		
	Region	CTL	NHE	$\frac{\text{NHE}-\text{CTL}}{CTL}\times 100$	CTL	NHE	$\frac{\text{NHE}-\text{CTL}}{CTL}\times 100$
GPH500 (gpm)	0-90°N	-12.825	-11.338	-11.59	25.263	23.984	-5.06
	60°N-90°N	-16.841	-11.590	-31.18	28.017	23.554	-15.93
SLP (hPa)	0-90°N	-0.522	-0.343	-34.29	2.714	2.515	-8.33
	60°N-90°N	-1.712	-1.079	-36.97	3.049	2.517	-17.45

337 Table 2. Mean bias and RMSE of the 500-hPa geopotential height (GPH500) and sea
338 level pressure (SLP) for the overall ten forecast days

		Mean Bias			RMSE		
	Region	CTL	NHE	$\frac{\text{NHE}-\text{CTL}}{CTL}\times 100$	CTL	NHE	$\frac{\text{NHE}-\text{CTL}}{CTL}\times 100$
GPH500 (gpm)	0-90°N	-7.923	-7.717	-2.6	16.455	16.369	-0.52
	60°N-90°N	-9.187	-8.438	-8.15	16.470	16.089	-2.31
SLP (hPa)	0-90°N	-0.107	-0.082	-23.46	1.87	1.841	-1.53
	60°N-90°N	-0.498	-0.411	-17.47	1.598	1.532	-4.13

339

340 Besides the GPH500, the forecast skill is also examined for the SLP in the NH.
341 As shown in Fig. 5a, the EXP_CTL experiment systematically underestimates the SLP
342 over East Asia and the Arctic, while overestimating SLP across North America and the
343 northern Atlantic. These biases are substantially corrected in the EXP_NHE experiment,
344 particularly in high-latitude regions north of 60°N (Fig. 5b). Similarly, the EXP_NHE
345 experiment firstly experiences a degradation in the early 6 days compared to EXP_CTL,
346 but it shows significant improvement at the end of the 10th forecast day, with the MB
347 reduced by 34.29% and the RMSE by 8.33%, respectively (Table 1). Greater decreases
348 of 36.97% (for MB) and 17.45% (for RMSE) are found in the high latitudes north of
349 60°N as well.

350

351

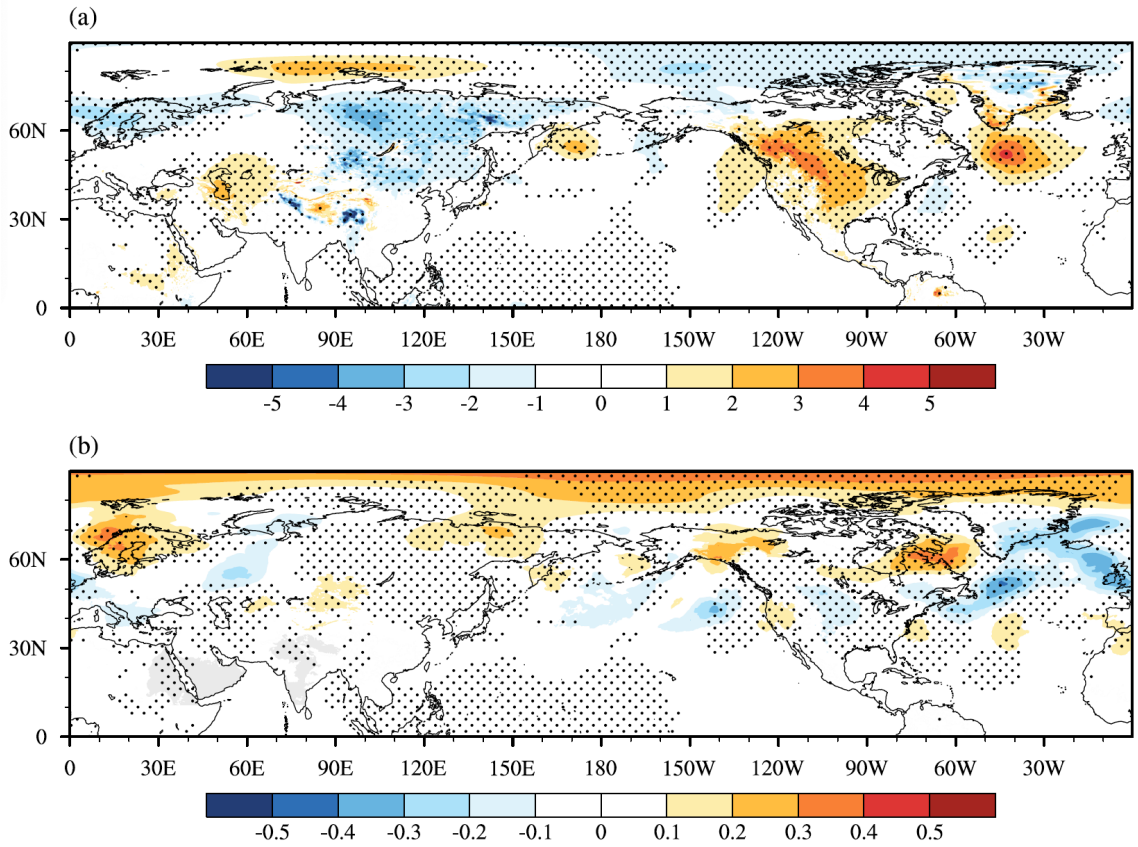

Figure 5. (a) Mean biases of SLP (shading; units: hPa) in the EXP_CTL experiment as compared to ERA5 averaged over the ten forecast days. (b) is similar to (a) but for the differences between the SLP (shading; units: hPa) in the EXP_CTL and EXP_NHE experiments (i.e., EXP_NHE minus EXP_CTL). Stippling in (a) and (b) denote differences statistically significant at the 95% confidence level.

From the above analyses, implementing the revised OGWD scheme in the high-resolution CMA-GFS model can help improve the medium range forecast of the NH large-scale circulation, especially in the high latitudes. In the next section, we will examine the underlying mechanisms responsible for the improvement of the circulation.

4. Physical interpretation

a. Changes of parameterized OGWD

The changes of wind circulation arise from the revision of the OGWD scheme. It is thus straightforward to study the parameterized OGWD in these two experiments. Figure 6a shows the vertical distribution of zonal-mean zonal OGWD averaged in the period of 10 December 2023 to 10 January 2024 in the EXP_CTL experiment. The differences between the parameterized OGWD in the two experiments (i.e., EXP_NHE minus EXP_CTL) are given in Fig. 6b. In boreal winter, there exists prominent OGWD in the stratosphere of the NH mid-to-high latitudes, which is favored by the decrease of air density with height (e.g., Lindzen, 1981) and the relatively weak winds between the tropospheric jet and polar night jet. The latter is called as the "valve layer" by Kruse et al. (2016). The maximum OGWD occurs between about 20 hPa and 1 hPa. In contrast, there is very weak OGWD in the SH stratosphere owing to the critical level absorption as mentioned above.

Compared to that in EXP_CTL, the zonal-mean zonal OGWD in EXP_NHE is generally weakened in the high latitudes of the NH (north of about 55°N), especially in the stratosphere (Fig. 6b). Note that the positive difference indicates a decrease of OGWD as the drag itself is negative. This is due to the fact that the NHE acts to decrease the surface WMF [see Eqs. (4) and (5)], i.e., the source of parameterized OGWs which determines the maximum wave momentum that can be deposited into the mean flow. Therefore, the decrease of surface WMF is prone to reduce the OGWD. Note that there is also enhancement of OGWD, e.g., in the stratosphere near 50°N. This may be attributed to a decrease in surface WMF, which suppresses tropospheric wave breaking

388 by lowering the gravity-wave amplitude limit for breaking at lower levels and thus
389 shifts the wave-breaking altitude upward. Consequently, a vertical structure
390 characterized by alternating positive-negative-positive anomalies from the surface to
391 the stratosphere would be expected. In consequence, more WMF is transported to the
392 stratosphere where the OGWs break owing to the decay of air density and lead to
393 stronger OGWD. This is similar to the redistribution of WMF in the vertical owing to
394 selective critical level filtering of OGWs in directional shear flows (Shutts, 1995; Xu
395 et al., 2012, 2019; van Niekerk et al., 2023). Generally, the changes in the vertical
396 structure of parameterized OGWD in the CMA-GFS model are similar to that in the
397 MPAS seasonal simulations conducted in Xu et al. (2024) which also considers the
398 NHE correction to the OGWD (cf. their Fig. 5). Instead, the lower-tropospheric OGWD
399 is also affected by the interaction and feedback between model dynamics and physical
400 parameterizations. Changes in the simulated low-level circulation, including possible
401 meridional displacement of drag-producing flow configurations, can modify the wind
402 speed, stability, and mountain-flow orientation sampled by the OGWD scheme, thereby
403 producing localized enhancement of the near-surface drag in EXP_NHE.

404

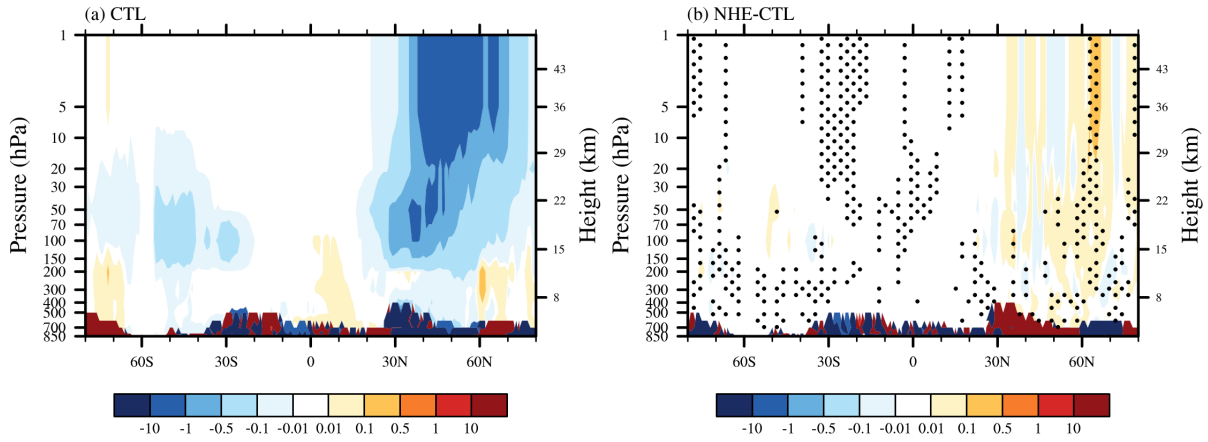

405

406 Figure 6. Vertical distributions of (a) zonal-mean zonal OGWD (units: m s^{-1} day^{-1})
407 averaged in the period of 10 December 2023 to 10 January 2024 obtained from
408 EXP_CTL, and (b) zonal-mean OGWD difference between the two experiments of
409 EXP_NHE and EXP_CTL (i.e., EXP_NHE minus EXP_CTL). Stippling in (b) denotes
410 differences statistically significant at the 95% confidence level.

411

412 The weakening of OGWD can directly increase the zonal winds in the polar
413 stratosphere and the mid-latitude troposphere of the NH, thus leading to a recover of
414 the weakened westerly jet. Conversely, the enhancement of OGWD can directly weaken
415 the zonal winds in the mid-latitude stratosphere and the polar troposphere of the NH,
416 thereby reducing the westerly biases (Figs. 1c, 1d). The parameterized OGWD in East
417 Asia is also examined to explain the changes of EASJ. As shown in Fig. 7a, there is
418 notable westward OGWD at 200 hPa in the high latitudes of East Asia where the
419 underlying terrain is very complex, such as the Taihang, Yanshan, Changbai, Greater
420 Khingan and Lesser Khingan Mountains. Thus, the largest easterly biases of the EASJ
421 occur in this region (Fig. 2c). When accounting for the NHE in the OGWD
422 parameterization scheme, the 200-hPa OGWD is mainly reduced (Fig. 7b). Clearly, the
423 enhanced EASJ is owing to the weakening of the parameterized OGWD.

424

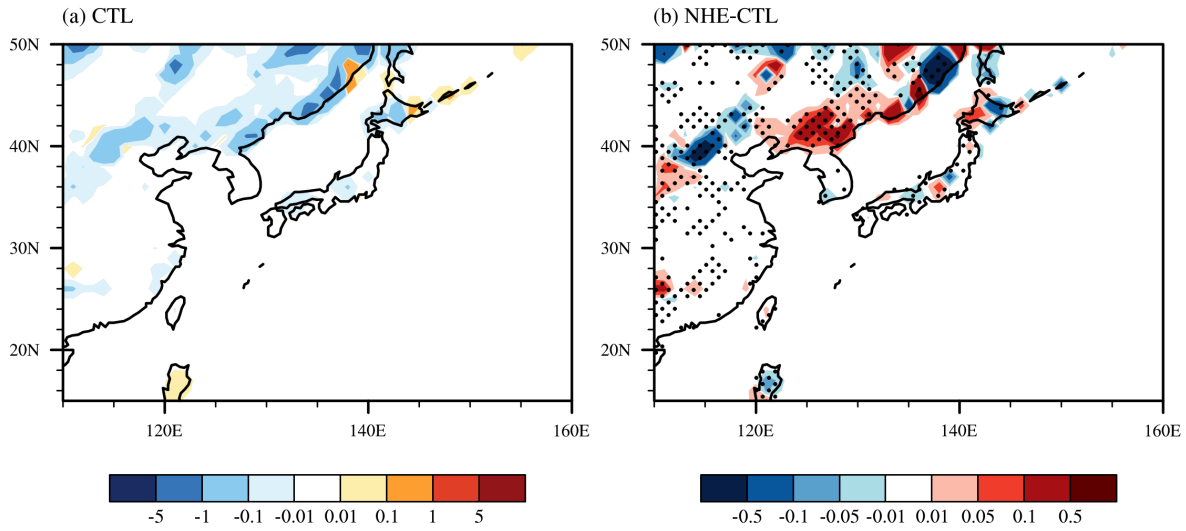

425

426 Figure 7. Horizontal distributions of (a) zonal OGWD (units: m s^{-1} day^{-1}) at 200 hPa
427 averaged in the period of 10 December 2023 to 10 January 2024 obtained from
428 EXP_CTL, and (b) zonal OGWD difference between the two experiments of EXP_NHE
429 and EXP_CTL (i.e., EXP_NHE minus EXP_CTL) at 200 hPa. Stippling in (b) denotes
430 differences statistically significant at the 95% confidence level.

431

432 *b. Resolved Rossby-wave adjustment*

433 In addition to the direct effect of the modified OGWD, the tropospheric response
434 in the Northern Hemisphere is also associated with an adjustment of resolved large-scale
435 Rossby waves. This interpretation is consistent with the wave-drag compensation and
436 propagation-adjustment mechanisms discussed in previous studies (e.g., Cohen et al., 2013;
437 Sigmond and Shepherd, 2014). In particular, changes in the background zonal wind may
438 alter the propagation conditions for planetary waves and thereby redistribute the resolved
439 wave forcing between the troposphere and stratosphere.

440 It is well known that the impacts of large-scale Rossby waves on the mean flow
441 can be measured by the convergence of the zonal-mean Eliassen-Palm (EP) flux. Figure
442 8a illustrates the distribution of the zonal-mean EP flux in the EXP_CTL experiment

443 which is calculated following Edmon et al. (1980). In the NH middle-to-high latitudes,
444 Rossby waves originate from the lower troposphere which propagate upward and
445 converge in the upper troposphere. These waves split into two branches in the lower
446 stratosphere. The first branch turns to propagate equatorward across the tropospheric
447 jet. The other branch continues to propagate upward to the upper stratosphere where
448 the EP flux is converged and decelerates the mean flow. As in the SH, the Rossby waves
449 cannot propagate into the stratosphere (not shown) because of the presence of easterlies
450 there during austral summer (Fig. 1a).

451 Figure 8b is similar to Fig. 8a but gives the differences between the zonal-mean
452 EP fluxes in the two experiments (i.e., EXP_NHE minus EXP_CTL). Compared to
453 EXP_CTL, the upward propagation of Rossby waves into the stratosphere is suppressed
454 in the high latitudes of the NH, leading to an enhanced convergence of EP flux in the
455 troposphere. As a result, the zonal-mean zonal winds in the NH polar troposphere are
456 decelerated by the large-scale Rossby wave forcing, which contributes to the alleviation
457 of westerly biases there (Figs. 1c, 1d). This may explain why the improvements in the
458 GPH 500 forecast emerge after 6 days in EXP_NHE (Fig. 2). The Rossby waves and
459 their interaction with the mean flow require several days to develop fully and influence
460 the large-scale circulation.

461

462

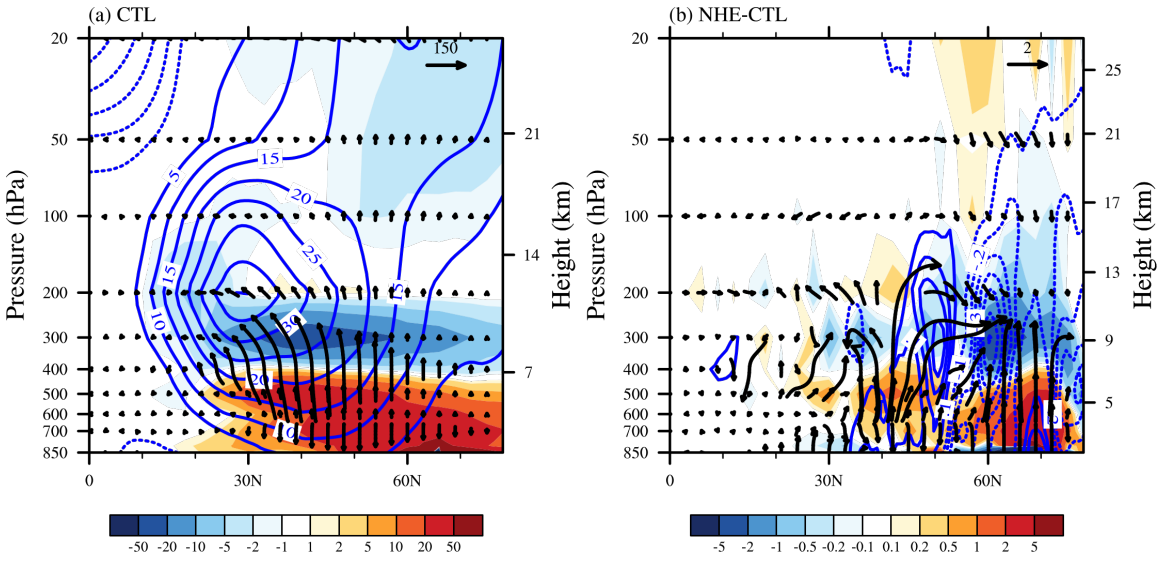

Figure 8. Vertical distributions of zonal-mean EP flux (vectors) and its divergence (shading; m s^{-1} day^{-1}) due to resolved waves averaged in the period of 10 December 2023 to 10 January 2024 obtained from (a) EXP_CTL, and (b) the difference between the two experiments of EXP_NHE and EXP_CTL (i.e., EXP_NHE minus EXP_CTL). Contours are the corresponding zonal-mean zonal wind (units: m s^{-1}).

The suppressed upward propagation of Rossby waves can be understood from the changes of the refractive index (*RFI*) that measures the ability of Rossby wave propagation (e.g., Chen and Robinson, 1992; Hu et al., 2019), which is defined as

$$RFI = \left[\frac{\overline{q_\varphi}}{r\bar{U}} - \left(\frac{k}{rcos\varphi}\right)^2 - \left(\frac{f}{2NH}\right)^2\right] r^2 , \quad (6)$$

where $\overline{U}$, k and H are the resolved zonal-mean zonal wind, zonal wave number and density scale height, respectively. $\overline{q_\varphi}$ represents the meridional gradient of the potential vorticity, which is expressed in the following form of

$$\overline{q_\varphi} = 2\Omega\cos\varphi - \left[\frac{(\bar{U}cos\varphi)_\varphi}{acos\varphi}\right]_\varphi + \frac{af^2}{R_d}\left(\frac{p\theta}{T}\frac{\overline{U_p}}{\overline{\theta_p}}\right)_p . \quad (7)$$

where Ω, θ and R_d being the Earth's angular frequency, potential temperature and dry gas constant, respectively. The subscripts φ and p represent the partial derivatives with respect to latitude and pressure, respectively. The overbars indicate temporal and zonal averages. From Eq. (6), the increase of zonal wind will narrow the range of Rossby wave numbers that can propagate into the stratosphere (Charney and Drazin, 1961; Xu et al., 2024).

As shown in Fig. 9, positive *RFI* values for both zonal wavenumbers 1 and 2 are found over the northern mid- to high latitudes in EXP_CTL, indicating that the basic-state flow is favorable for the upward propagation of planetary waves (Figs. 9a, 9c). In EXP_NHE, however, the *RFI* is generally reduced over the same region, especially in the upper troposphere and lower stratosphere. These negative *RFI* anomalies suggest that the strengthened background westerlies in the polar stratosphere make the environment less conducive to the vertical propagation of Rossby waves (Figs. 9b, 9d). Similar behavior is found for both wavenumber-1 and wavenumber-2 components, although the wavenumber-1 signal appears more spatially coherent. Therefore, the reduction of *RFI* provides a dynamical explanation for the weakened upward EP-flux branch seen in Fig. 8b.

Physically, the revised OGWD scheme weakens the parameterized drag in the northern polar stratosphere, which strengthens the local westerlies. Stronger background westerlies narrow the range of planetary-wave numbers that can propagate vertically into the stratosphere. Consequently, the upward propagation of resolved Rossby waves is suppressed, and less resolved wave forcing reaches the polar

stratosphere. This effect acts together with the weakened parameterized OGWD to reduce the easterly wind bias in the polar stratosphere. At the same time, the associated redistribution of resolved wave forcing favors a weakening of the polar-tropospheric westerlies, thereby contributing to the improvement of the large-scale circulation over the northern high latitudes.

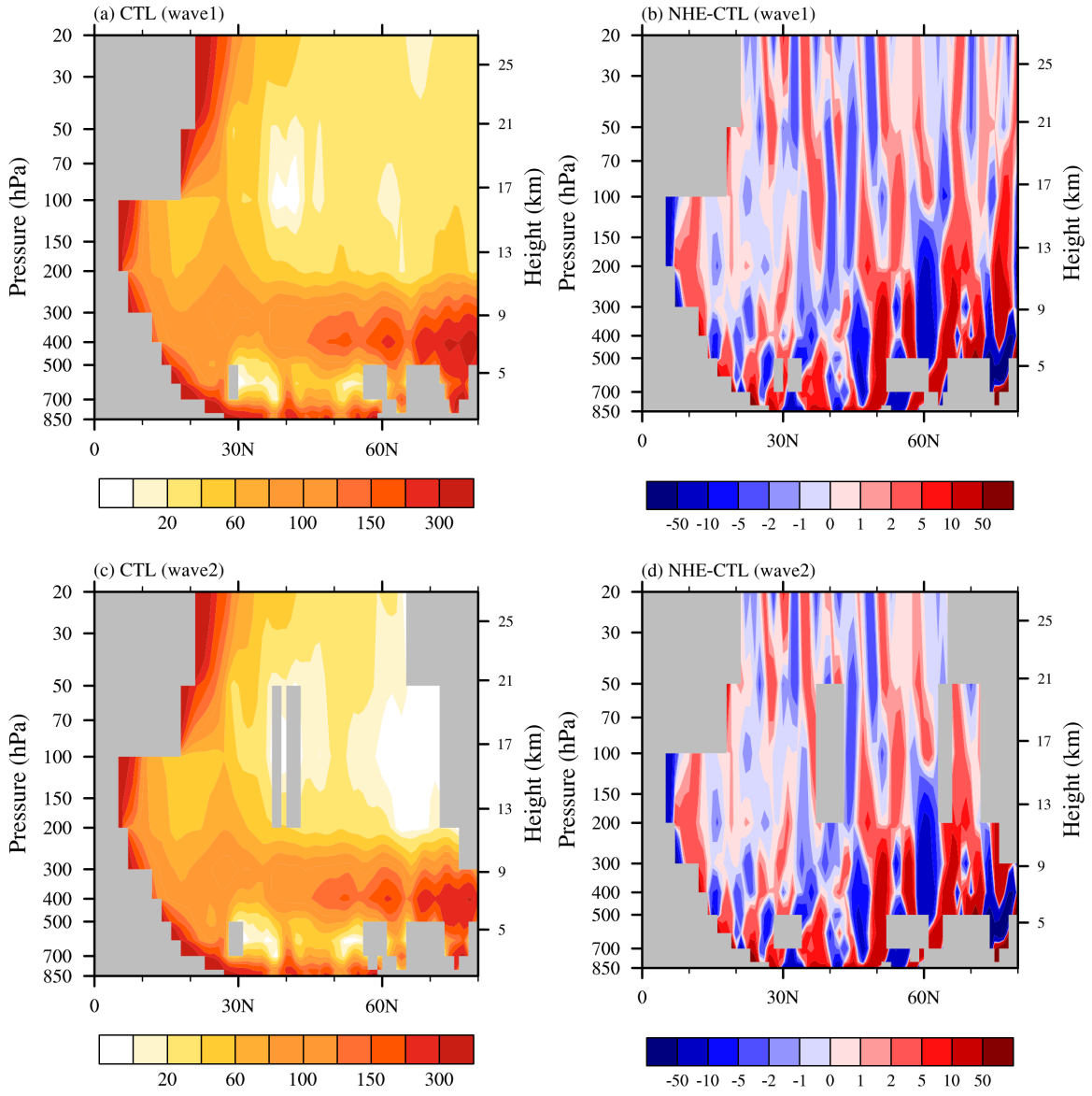

Figure 9. Refractive index for the (a) wavenumber-1 and (c) wavenumber-2 resolved waves averaged over the period of 10 December 2023 to 10 January 2024 in the

EXP_CTL experiment. (b) The difference between the refractive indices of wavenumber 1 in EXP_NHE and EXP_CTL (EXP_NHE minus EXP_CTL). (d) As in (b), but for wavenumber 2.

To provide a more robust diagnosis of the bulk propagation conditions, the zonal-mean refractive-index diagnostic averaged over 50°-80°N is further presented in Fig. 10. The averaged *RFI* anomalies are positive mainly below about 500 hPa, whereas negative anomalies dominate above 500 hPa for both wavenumber 1 and wavenumber 2. This vertical contrast is consistent with the EP-flux response in Fig. 8b. The lower-tropospheric environment tends to favor the initial upward propagation of resolved Rossby waves, while the upper-tropospheric and lower-stratospheric background state becomes less favorable for their continued propagation into the stratosphere.

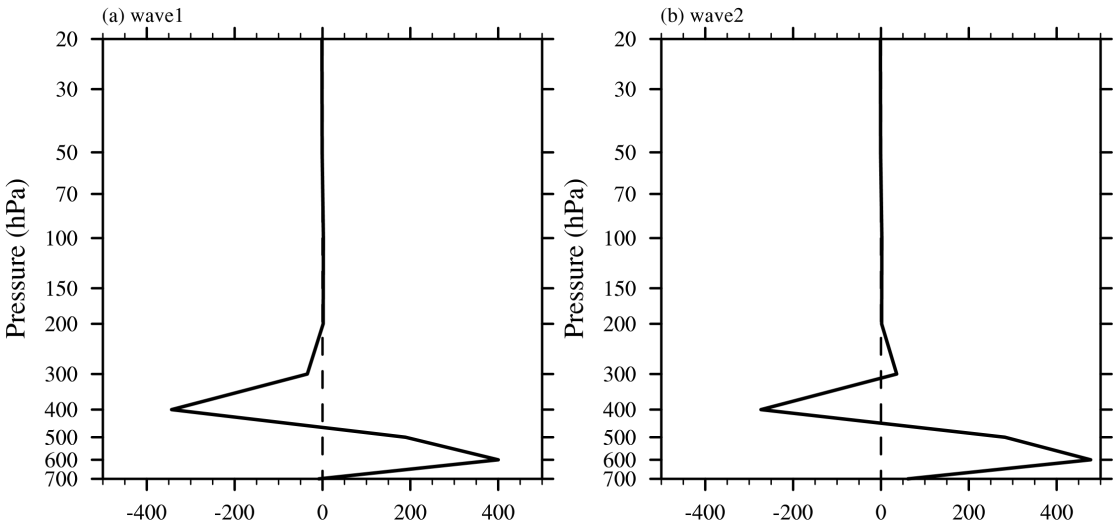

Figure 10. (a) The difference between the refractive indices of wavenumber 1 in EXP_NHE and EXP_CTL (EXP_NHE minus EXP_CTL), averaged over 50°-80°N. (b) as in (a), but for wavenumber 2.

5. Summary and discussions

The latest China Meteorological Administration Global Forecast System (CMA-GFS) v4.0 model has been upgraded to a higher resolution of 0.125° in 2023. However,

this high-resolution global model still uses the parameterization scheme of orographic gravity wave drag (OGWD) developed by Kim and Arakawa (1995; KA95) which is based on hydrostatic orographic gravity wave (OGW) theory. In this study, the KA95 OGWD scheme is revised by taking into account the nonhydrostatic effect (NHE) on the surface wave momentum flux (WMF) of OGWs, according to the nonhydrostatic OGW theory derived in our earlier study of Xu et al. (2021). The performance of the revised OGWD scheme is then evaluated for the medium-range forecast of the CMA-GFSv4.0 model. Two sets of numerical experiments (i.e., EXP_CTL and EXP_NHE) are conducted by using the original KA95 scheme and the revised NHE scheme, respectively. In each numerical experiment, there are in total 31 forecasts of 10-day forecasts. In each numerical experiment, there are in total 31 independent 10-day forecasts which are initiated at 00 UTC on each day of December 2023.

The results show that the revised OGWD scheme can improve the medium-range forecast of large-scale circulation in the Northern Hemisphere (NH), especially in the high latitudes. The easterly biases of zonal-mean zonal wind in the NH stratosphere are reduced, with both the magnitude and location of the polar night jet being better captured. The underestimation of the East Asia subtropical jet (EASJ) is also alleviated. In contrast, the revised OGWD scheme shows little influence on the stratospheric circulation in the Southern Hemisphere (SH). This is because, in boreal winter (i.e., austral summer), there is hardly OGWD in the SH stratosphere owing to the effect of critical-level absorption, leading to comparatively smaller circulation responses. Therefore, the quantitative evaluation of forecast skill is mainly performed

for the NH, where the impact of the revised OGWD scheme is physically more pronounced and statistically more robust.

Quantitative evaluation is performed for the medium-range forecast skills in the NH, taking the ERA5 reanalysis dataset as reference. Both experiments showed lower geopotential height (GPH) at 500 hPa than ERA5 reanalysis, with the mean bias (MB) and root mean square error (RMSE) increasing with forecast lead time. EXP_NHE initially has greater MB and RMSE than EXP_CTL until the 6th forecast day, but these metrics decrease more rapidly afterwards, resulting in an 11.59% reduction in MB and a 5.06% reduction in RMSE by day 10. Over the total 10 forecast days, the MB and RMSE of the GPH 500 in the NH are reduced by 2.6% and 0.52%, respectively, indicating improved simulation of large-scale circulation in the NH. The improvement is more noticeable in the high latitudes north of about 60°N, where the MB and RMSE of GPH 500 are decreased by 31.18% and 15.93% at the 10th forecast day. Similar results are found for the sea level pressure (SLP) in the NH, the MB and RMSE of which are reduced by 34.29% and 8.33%, respectively, by day 10 in EXP_NHE.

The dynamics responsible for the improvement of large-scale wind circulation are examined. The NHEs act to decrease the surface WMF of OGWs, which leads to a general weakening of the parameterized OGWD in the midlatitudes and high latitudes of the NH. This weakening of OGWD directly increases the zonal winds in the mid-latitude troposphere and polar stratosphere, reducing the easterly biases. The enhanced zonal wind in the polar stratosphere acts to narrow the range of large-scale Rossby wave numbers that can propagate into the stratosphere by reducing the refractive index of Rossby waves. The suppressed upward propagation of Rossby waves leads to greater convergence of

Eliassen-Palm (EP) flux (i.e., resolved wave forcing) in the NH polar troposphere, which decelerates the zonal winds and thus alleviates the westerly biases there.

To sum up, this study demonstrates that incorporating the NHE into the OGWD parameterization scheme can help improve the simulation of large-scale atmospheric circulation in high-resolution global NWP models, which is thus important for accurate weather forecasts and/or climate simulations. However, there are still some limitations in this work. For example, this study pays much attention to the medium-range forecast of large-scale circulation in winter of NH. To further validate its effectiveness and robustness, it is necessary to conduct more comprehensive evaluations of the nonhydrostatic OGWD scheme in various numerical models focusing on different weather and climate systems. Additionally, this work only takes into account the effects of NHE on the OGWD. Other factors such as the vertical wind shear and moisture could also greatly affect the OGWD (e.g., Xu et al., 2019; Xu et al., 2020; Wang et al., 2025; Zhang et al., 2025). While Xu et al. (2021) explored the nonhydrostatic OGWs generated in a constant flow, it remains unclear how the vertical wind shear and moisture affects the behavior of nonhydrostatic OGWs which needs further study.

Code and data availability. The China Meteorological Administration Global Forecast System (CMA-GFS) model is archived on Zenodo under https://doi.org/10.5281/zenodo.18476721 (Zhang, 2026). The CMA-GFS outputs and the ERA5 reanalysis data used for the comparison, along with the codes for orographic gravity wave scheme are uploaded to https://doi.org/10.5281/zenodo.18529537 (Zhang, 2026).

Author contributions. RRZ was responsible for formal analysis, writing the original draft and visualization. ZZA carried out data analyses. XX developed the code and conducted the analysis. HLX and QYC provided the resources and data curation.

Competing interests. The contact author has declared that none of the authors has any competing interests.

Acknowledgements. The authors would like to express their sincere thanks to the anonymous referees.

Financial support. This work is mainly supported by the National Natural Science Foundation of China (grants no. U2342226, 42275163), the Joint Research Project for Meteorological Capacity Improvement (grant no. 22NLTSZ006), and Jiangsu Meteorological Observatory (grant no. KQ202502).

References

Alexander, M. J., Geller, M., McLandress, C., Polavarapu, S., Preusse, P., Sassi, F., Sato, K., Eckermann, S., Ern, M., Hertzog, A., Kawatani, Y., Pulido, M., Shaw, T.A., Sigmond, M., Vincent, R. and Watanabe, S.: Recent developments in gravity-wave effects in climate models and the global distribution of gravity-wave momentum flux from observations and models, Quarterly Journal of the Royal Meteorological Society, 136, 1103-1124, https://doi.org/10.1002/qj.637, 2010.

Alpert, J.: Sub-grid scale mountain blocking at NCEP, 20th Conference on Weather Analysis and Forecasting/16th Conference on Numerical Weather Prediction, https://ams.confex.com/ams/84Annual/techprogram/program_185.htm, 2004.

Beljaars, A. C. M., Brown, A. R., and Wood, N.: A new parametrization of turbulent orographic form drag, Quarterly Journal of the Royal Meteorological Society, 130, 1327-1347, https://doi.org/10.1256/qj.03.73, 2004.

Booker, J. R., and Bretherton, F. P.: The critical layer for internal gravity waves in a shear flow, Journal of Fluid Mechanics, 27, 513-539, https://doi.org/10.1017/S0022112067000515, 1967.

Charney, J. G., and Drazin, P. G.: Propagation of planetary-scale disturbances from the lower into the upper atmosphere, Journal of Geophysical Research (1896-1977), 66, 83-109, https://doi.org/10.1029/JZ066i001p00083, 1961.

Chen, J., Ma, Z., Li, Z., Shen, X., Su, Y., Chen, Q., and Liu, Y.: Vertical diffusion and cloud scheme coupling to the Charney-Phillips vertical grid in GRAPES global forecast system, Quarterly Journal of the Royal Meteorological Society, 146, 2191-2204, https://doi.org/10.1002/qj.3787, 2020.

636 Chen Q., Shen, X., Sun, J., and Liu, K.: Momentum budget diagnosis and the
637 parameterization of subgrid-scale orographic drag in global GRAPES, Journal of
638 Meteorological Research, 30, 771-788, https://doi.org/10.1007/s13351-016-6033-
639 y, 2016.
640 Chen, P., and Robinson, W. A.: Propagation of Planetary Waves between the Troposphere
641 and Stratosphere, Journal of Atmospheric Sciences, 49, 2533-2545,
642 https://doi.org/10.1175/1520-0469(1992)049<2533:POPWBT>2.0.CO;2, 1992.
643 Choi, H. J., and Hong, S. Y.: An updated subgrid orographic parameterization for global
644 atmospheric forecast models, Journal of Geophysical Research: Atmospheres, 120,
645 12445-12457, https://doi.org/10.1002/2015JD024230, 2015.
646 Cohen, N. Y., Gerber, E. P., and Buhler, O.: Compensation between resolved and
647 unresolved wave driving in the stratosphere: Implications for downward control,
648 Journal of the Atmospheric Sciences, 70, 3780-3798, https://doi.org/10.1175/JAS-
649 D-12-0346.1, 2013.
650 Dai, Y., Zeng, X., Robert, E. D., Baker, L., Bonan, G. B., Bosilovich, M. G., Denning A.
651 S., Dirmeyer, P. A., Houser, P. R., Niu, G., Oleson, K. W., Schlosser, C. A., Yang,
652 Z.: The Common Land Model, Bulletin of the American Meteorological Society,
653 84, 1013-1024, https://doi.org/10.1175/BAMS-84-8-1013, 2003.
654 Edmon, H. J., Hoskins, B. J. and McIntyre, M. E.: Eliassen-Palm Cross Sections for the
655 Troposphere, Journal of Atmospheric Sciences, 37, 2600-2616,
656 https://doi.org/10.1175/1520-0469(1980)037<2600:EPCSFT>2.0.CO;2, 1980.

657 Fritts, D. C., and Alexander, M. J.: Gravity wave dynamics and effects in the middle
658 atmosphere, Reviews of Geophysics, 41, https://doi.org/10.1029/2001RG000106,
659 2003.
660 Han, J., and Pan, H. L.: Revision of Convection and Vertical Diffusion Schemes in the
661 NCEP Global Forecast System, Weather and Forecasting, 26, 520-533,
662 https://doi.org/10.1175/WAF-D-10-05038.1, 2011.
663 Haynes, P. H., Mclntyre, M. E., Shepherd, T. G., Marks, C. J., and Shine, K. P.: On the
664 "Downward Control" of Extratropical Diabatic Circulations by Eddy-Induced
665 Mean Zonal Forces, Journal of Atmospheric Sciences, 48, 651-678,
666 https://doi.org/10.1175/1520-0469(1991)048<0651:OTCOED>2.0.CO;2, 1991.
667 Hersbach, H., Bell, B., Berrisford, P., et al: The ERA5 global reanalysis, Quarterly Journal
668 of the Royal Meteorological Society, 146, 1999-2049,
669 https://doi.org/10.1002/qj.3803, 2020.
670 Hong, S. Y., and Pan, H. L.: Nonlocal Boundary Layer Vertical Diffusion in a Medium-
671 Range Forecast Model, Monthly Weather Review, 124, 2322-2339,
672 https://doi.org/10.1175/1520-0493(1996)124<2322:NBLVDI>2.0.CO;2, 1996.
673 Hu, D., Guo, Y., and Guan, Z.: Recent Weakening in the Stratospheric Planetary Wave
674 Intensity in Early Winter, Geophysical Research Letters, 46, 3953-3962,
675 https://doi.org/10.1029/2019GL082113, 2019.
676 Kim, Y. J.: Balance of drag between the middle and lower atmospheres in a global
677 atmospheric forecast model, Journal of Geophysical Research: Atmospheres, 112,
678 https://doi.org/10.1029/2007JD008647, 2007.

679 Kim, Y. J., and Arakawa, A.: Improvement of Orographic Gravity Wave Parameterization
680 Using a Mesoscale Gravity Wave Model, Journal of Atmospheric Sciences, 52,
681 1875-1902, https://doi.org/10.1175/1520-
682 0469(1995)052<1875:IOOGWP>2.0.CO;2, 1995.
683 Kim, Y. J., and Doyle, J. D.: Extension of an orographic-drag parametrization scheme to
684 incorporate orographic anisotropy and flow blocking, Quarterly Journal of the
685 Royal Meteorological Society, 131, 1893-1921, https://doi.org/10.1256/qj.04.160,
686 2005.
687 Kim, Y. J., Eckermann, S., and Chun, H. Y.: An overview of the past, present and future
688 of gravity-wave drag parametrization for numerical climate and weather prediction
689 models - Survey article, Atmosphere-ocean, 41, 65-98,
690 https://doi.org/10.3137/ao.410105, 2003.
691 Klemp, J. B., and Durran, D. R.: An Upper Boundary Condition Permitting Internal Gravity
692 Wave Radiation in Numerical Mesoscale Models, Monthly Weather Review, 111,
693 430-444, https://doi.org/10.1175/1520-0493(1983)111<0430:AUBCPI>2.0.CO;2,
694 1983.
695 Kruse, C. G., Smith, R. B., and Eckermann, S. D.: The Midlatitude Lower-Stratospheric
696 Mountain Wave “Valve Layer”, Journal of the Atmospheric Sciences, 73, 5081-
697 5100, https://doi.org/10.1175/JAS-D-16-0173.1, 2016.
698 Li, M., Xu, X., Teixeira, M. A. C., Xue, M., Xue, H., Zhu, K., and Huang, H.: Improved
699 Orographic Gravity Wave Drag Parameterization Accounting for the
700 Nonhydrostatic Effect in the Weather Research and Forecasting Model: Tests for

Short-Range Forecast of Northeast China Cold Vortices, Monthly Weather Review, 152, 2623-2637, https://doi.org/10.1175/MWR-D-24-0097.1, 2024.

Li, R., Xu, X., Xu, X., Shepherd, T. G., and Wang, Y.: Importance of orographic gravity waves over the Tibetan Plateau on the spring rainfall in East Asia, Science China Earth Sciences, 66, 2594-2602, https://doi.org/10.1007/s11430-023-1204-6, 2023.

Lindzen, R. S.: Turbulence and stress owing to gravity wave and tidal breakdown, Journal of Geophysical Research: Oceans, 86, 9707-9714, https://doi.org/10.1029/JC086iC10p09707, 1981.

Liu, K., Chen, Q., and Sun, J.: Modification of cumulus convection and planetary boundary layer schemes in the GRAPES global model, Journal of Meteorological Research, 29, 806-822, https://doi.org/10.1007/s13351-015-5043-5, 2015.

Lott, F., and Miller, M. J.: A new subgrid-scale orographic drag parametrization: Its formulation and testing, Quarterly Journal of the Royal Meteorological Society, 123, 101-127, https://doi.org/10.1002/qj.49712353704, 1997.

Lu, Y., Wu, T., Xu, X., Zhang, L., and Chu, M.: Improved Simulation of the Antarctic Stratospheric Final Warming by Modifying the Orographic Gravity Wave Parameterization in the Beijing Climate Center Atmospheric General Circulation Model, Atmosphere, 11, 576, https://doi.org/10.3390/atmos11060576, 2020.

Lu, Y., Xu, X., Wang, L., Liu, Y., Wu, T., Jie, W., and Sun, J.: Machine Learning Emulation of Subgrid-Scale Orographic Gravity Wave Drag in a General Circulation Model with Middle Atmosphere Extension, J. Adv. Model. Earth Syst., 16, e2023MS003611, https://doi.org/10.1029/2023MS003611, 2024.

723 Ma, Z., Liu, Q., Zhao, C., Shen, X., Wang, Y., Jiang, J. H., Zhe, L., and Yung, Y.:
724 Application and Evaluation of an Explicit Prognostic Cloud-Cover Scheme in
725 GRAPES Global Forecast System, Journal of Advances in Modeling Earth Systems,
726 10, 652-667, https://doi.org/10.1002/2017MS001234, 2018.
727 McFarlane, N. A.: The Effect of Orographically Excited Gravity Wave Drag on the General
728 Circulation of the Lower Stratosphere and Troposphere, Journal of Atmospheric
729 Sciences, 44, 1775-1800, https://doi.org/10.1175/1520-
730 0469(1987)044<1775:TEOOEG>2.0.CO;2, 1987.
731 McLandress, C., Shepherd, T. G., Polavarapu, S., and Beagley, S. R.: Is Missing
732 Orographic Gravity Wave Drag near 60°S the Cause of the Stratospheric Zonal
733 Wind Biases in Chemistry-Climate Models? Journal of the Atmospheric Sciences,
734 69, 802-818, https://doi.org/10.1175/JAS-D-11-0159.1, 2012.
735 Miller, M. J., and Palmer, T. N.: Orographic gravity wave drag: Its parameterization and
736 influence in general circulation and numerical weather prediction models,
737 Presented at the ECWMF Workshop on Observation, Theory and Modelling of
738 Orographic Effects 1, 283-333, 1986.
739 Morcrette, J. J., Barker, H. W. J., Cole, N. S., Iacono, M. J., and Pincus, R.: Impact of a
740 New Radiation Package, McRad, in the ECMWF Integrated Forecasting System,
741 Monthly Weather Review, 136, 4773-4798,
742 https://doi.org/10.1175/2008MWR2363.1, 2008.
743 Palmer, T. N., Shutts, G. J., and Swinbank, R.: Alleviation of a systematic westerly bias in
744 general circulation and numerical weather prediction models through an orographic

gravity wave drag parametrization, Quarterly Journal of the Royal Meteorological Society, 112, 1001-1039, https://doi.org/10.1002/qj.49711247406, 1986.

Scinocca, J., and McFarlane, N.: The parametrization of drag induced by stratified flow over anisotropic orography, Quarterly Journal of the Royal Meteorological Society, 126, 2353-2393, https://doi.org/10.1002/qj.49712656802, 2000.

Shen, X., Su, Y., Hu, J., et al.: Development and Operation Transformation of GRAPES Global Middle-range Forecast System, Journal of Applied Meteorological Science, 28, 1-10, https://doi.org/10.11898/1001-7313.20170101, 2017.

Shen, X., Wang, J., Li, Z., Chen, D., and Gong, J.: Research and operational development of numerical weather prediction in China, Journal of Meteorological Research, 34, 675-698, https://doi.org/10.1007/s13351-020-9847-6, 2020.

Shen, X. S., Su, Y., Zhang, H. L., et al.: New version of the CMA-GFS dynamical core based on the predictor-corrector time integration scheme, Journal of Meteorological Research, 37, 273-285, https://doi.org/10.1007/s13351-023-3002-0, 2023.

Shutts, G.: Gravity-wave drag parametrization over complex terrain: The effect of critical-level absorption in directional wind-shear, Quarterly Journal of the Royal Meteorological Society, 121, 1005-1021, https://doi.org/10.1002/qj.49712152504, 1995.

Sigmond, M., and Shepherd, T. G.: Compensation between resolved wave driving and parameterized orographic gravity wave driving of the Brewer-Dobson circulation and its response to climate change, Journal of Climate, 27, 5601-5610, https://doi.org/10.1175/JCLI-D-13-00644.1, 2014.

767 Smith, R. B.: The Influence of Mountains on the Atmosphere, In B. Saltzman (Ed.),
768 Advances in Geophysics (Vol. 21, pp. 87-230): Elsevier, 1979.
769 Teixeira, M. A. C.: The physics of orographic gravity wave drag, Frontiers in Physics, 2,
770 https://doi.org/10.3389/fphy.2014.00043, 2014.
771 van Niekerk, A., Vosper, S. B., and Teixeira, M. A. C.: Accounting for the three-
772 dimensional nature of mountain waves: Parametrising partial critical-level filtering,
773 Quarterly Journal of the Royal Meteorological Society, 149, 515-536,
774 https://doi.org/10.1002/qj.4421, 2023.
775 Wang, Y., Xu, X., Yang, X., Wei, P., Li, C., Wu, J., and Ren, K.: Moist Orographic Gravity
776 Wave Drag Parameterization Reduces Wet Bias of Summer Rainfall Over Tibetan
777 Plateau, npj Climate and Atmospheric Science, 8, 367,
778 https://doi.org/10.1038/s41612-025-01245-z, 2025.
779 Wei, P., Xu, X., Xue, M., Li, J., Zhao, K., and Zhang, Q.: Complex Terrain Causes Global
780 Model Prediction Biases of 21.7 Zhengzhou Extreme Precipitation, Science
781 Bulletin, https://doi.org/10.1016/j.scib.2025.09.015, 2025.
782 Xu, X., Zhou, X., Yang, K., Lu, Y., Zhang, R., Yang, B., Tang, J., and Wang, Y.:
783 Reducing Winter Precipitation Biases Over the Western Tibetan Plateau in the
784 Model for Prediction Across Scales (MPAS) With a Revised Parameterization of
785 Orographic Gravity Wave Drag, Journal of Geophysical Research: Atmospheres,
786 128, e2023JD039123, https://doi.org/10.1029/2023JD039123, 2023.
787 Xu, X., Li, R., Teixeira, M. A. C., and Lu, Y.: On the Momentum Flux of Vertically
788 Propagating Orographic Gravity Waves Excited in Nonhydrostatic Flow over

789 Three-Dimensional Orography, Journal of the Atmospheric Sciences, 78, 1807-
790 1822, https://doi.org/10.1175/JAS-D-20-0370.1, 2021.
791 Xu, X., Teixeira, M. A. C., Xue, M., Lu, Y., and Tang, J.: Impacts of wind profile shear
792 and curvature on the parameterized orographic gravity wave stress in the Weather
793 Research and Forecasting model, Quarterly Journal of the Royal Meteorological
794 Society, 146, 3086-3100, https://doi.org/10.1002/qj.3828, 2020.
795 Xu, X., Wang, Y., and Xue, M.: Momentum Flux and Flux Divergence of Gravity Waves
796 in Directional Shear Flows over Three-Dimensional Mountains, Journal of the
797 Atmospheric Sciences, 69, 3733-3744, https://doi.org/10.1175/JAS-D-12-044.1,
798 2012.
799 Xu, X., Xue, M., Teixeira, M. A. C., Tang, J., and Wang, Y.: Parameterization of
800 Directional Absorption of Orographic Gravity Waves and Its Impact on the
801 Atmospheric General Circulation Simulated by the Weather Research and
802 Forecasting Model, Journal of the Atmospheric Sciences, 76, 3435-3453,
803 https://doi.org/10.1175/JAS-D-18-0365.1, 2019.
804 Xu, X., Zhang, R., Teixeira, M. A. C., van Niekerk, A., Xue, M., Lu, Y., Xue, H., Li, R.,
805 Wang, Y.: A Parameterization Scheme Accounting for Nonhydrostatic Effects on
806 the Momentum Flux of Vertically Propagating Orographic Gravity Waves:
807 Formulas and Preliminary Tests in the Model for Prediction Across Scales (MPAS),
808 Journal of the Atmospheric Sciences, 81, 805-817, https://doi.org/10.1175/JAS-D-
809 23-0020.1, 2024.

Xue, H., Shen, X., and Su, Y.: Parameterization of Turbulent Orographic Form Drag and Implementation in GRAPES, Journal of Applied Meteorological Science, 22, 169-181, http://qikan.camscma.cn/en/article/id/20110206, 2011.

Zängl, G.: Orographic Gravity Waves Close to the Nonhydrostatic Limit of Vertical Propagation, Journal of the Atmospheric Sciences, 60, 2045-2063, https://doi.org/10.1175/1520-0469(2003)060<2045:OGWCTT>2.0.CO;2, 2003.

Zhang, R.: CMA-GFS Model. Zenodo [code], https://doi.org/10.5281/zenodo.18476721, 2026.

Zhang, R.: CMA-GFS outputs. Zenodo [data set], https://doi.org/10.5281/zenodo.18529537, 2026.

Zhang, R., Lu, Y., Xu, X., and Wang, Y.: Impacts of wind profile shear and curvature on the parameterized orographic gravity wave stress in a middle atmosphere resolving general circulation model, Journal of Advances in Modeling Earth Systems, 17, e2024MS004232, https://doi.org/10.1029/2024MS004232, 2025.

Zhang, R., Xu, X., and Wang, Y.: Impacts of Subgrid Orographic Drag on the Summer Monsoon Circulation and Precipitation in East Asia, Journal of Geophysical Research: Atmospheres, 125, e2019JD032337, https://doi.org/10.1029/2019JD032337, 2020.

Zhong, S., and Chen, Z.: Improved wind and precipitation forecasts over South China using a modified orographic drag parameterization scheme, Journal of Meteorological Research, 29, 132-143, https://doi.org/10.1007/s13351-014-4934-1, 2015.